

# Nonlocal fluxes and Stokes drift effects in the K-profile parameterization.

William D. Smyth<sup>1</sup>, Eric D. Skyllingstad<sup>1</sup>, Gregory B. Crawford<sup>2</sup> and Hemantha Wijesekera<sup>1</sup>

<sup>1</sup> College of Oceanic and Atmospheric Sciences  
Oregon State University, Corvallis, OR 97331-5503

<sup>2</sup> Department of Oceanography  
Humboldt State University, Arcata, CA 95521-8299

Communicating author: W.D. Smyth, [smyth@coas.oregonstate.edu](mailto:smyth@coas.oregonstate.edu),  
telephone: (541) 737-3029, fax: (541) 737-2064.

Submitted August 30th, 2001.

## Abstract

The K-profile parameterization of upper ocean mixing is tested and extended using observations and large eddy simulations of upper ocean response to a westerly wind-burst. A nonlocal momentum flux term is added, and the amplitude of the nonlocal scalar flux is recalibrated. Parameterizations of Stokes drift effects are added following recent work by McWilliams and Sullivan (2001). These changes allow the parameterization to produce both realistic gradients of momentum and scalars in the nocturnal boundary layer and enhanced mixing during stable conditions. The revised parameterization is expected to produce improved representations of lateral advection and sea-surface temperature in large-scale models.

Key Words: ocean modeling, turbulence, mixed layer, K-profile parameterization, KPP.

## 1 Introduction

A central goal of ocean turbulence research is the development of efficient, accurate parameterizations of vertical mixing for use in large-scale models. Currently popular approaches include the Mellor-Yamada hierarchy of models (e.g. Mellor and Yamada, 1982; Kantha and Clayson, 1994), the  $k-\epsilon$  model (e.g. Burchard et al., 1998) and the nonlocal K-profile parameterization (KPP), introduced by Large et al. (1994; hereafter LMD). Every mixing parameterization represents a compromise between accuracy and efficiency. Of the currently popular models, the KPP is the most efficient; it forsakes theoretical development almost entirely in favor of simple, empirical representations of specific processes. The result is a scheme that involves no evolution equations and is therefore extremely cheap in terms of computer cycles and memory. In contrast, more accurate schemes such as the  $k-\epsilon$  model require storage and transport operations for two turbulence quantities in addition to the usual hydrodynamic field variables. Computational efficiency is crucial in large-scale models, where the need to resolve mesoscale eddies puts extreme demands on computer capacity.

Since its introduction, the KPP has undergone significant refinement (e.g. Large and Gent 1999; McWilliams

and Sullivan 2001, hereafter MS), both in terms of adding new processes to the model and refining the empirical constants that quantify those processes. Here, we further this effort via comparisons with both observations and large eddy simulations (LES) of upper ocean structure during a westerly windburst in the equatorial Pacific Ocean. Of particular interest to us are “nonlocal” vertical property fluxes and Stokes drift effects.

Nonlocal fluxes are driven by eddies on scales comparable to or larger than the vertical scale over which the background shear and stratification change. In the nocturnal boundary layer, for example, net surface cooling generates a mean density gradient which is unstable near the surface, nearly zero within the mixed layer, and strongly stable in the entrainment zone at the base of the mixed layer. Convective plumes carry property fluxes that depend on the net buoyancy change across the mixed layer, and therefore have little relationship to the local gradient at any particular depth. Such fluxes can be strong even in the mixed layer interior, where the background gradients are near zero. Parameterization of these fluxes using the standard gradient-diffusion formalism is clearly inappropriate.

Improper representation of nonlocal fluxes promotes excessively strong vertical gradients within the mixed layer, as we will show. This consequence is not the worst that could be envisioned, as it allows the net property fluxes across the boundary layer to be represented with reasonable accuracy. Nevertheless, the deficiency is potentially serious. For example, excessive shear in the mixed layer leads to unrealistic lateral advection in a large scale model. Unrealistic values for surface currents can lead to major errors in regions with strong fronts, such as coastal boundaries and near western boundary currents (e.g. the Gulf Stream), and any region of the ocean with strong wind-driven circulations (e.g. coastal upwelling). Increased mixing of momentum by nonlocal fluxes can also alter the entrainment rate at the mixed layer base, thereby changing the bulk characteristics of the upper ocean.

The meteorological community has studied nonlocal fluxes in the atmospheric boundary layer (ABL) extensively (e.g. Deardorff, 1972; Mailhot and Benoit, 1982; Therry and Lacarrere, 1983; Troen and Mahrt, 1986; Holtzlag and Moeng, 1991; Frech and Mahrt, 1995; Brown and Grant, 1997), and has developed useful formalisms for their incorporation into atmospheric models. LMD took advantage of the similarity between the ABL and the

upper ocean boundary layer (OBL) to bring meteorological experience to bear on the ocean problem, and thereby provided for the inclusion of nonlocal fluxes in the KPP. At present, this effort is far from complete. While useful mathematical representations for nonlocal fluxes have been developed, sensitivity experiments are needed to establish proper values for the adjustable parameters. Even in the atmospheric context there have been few such studies, and the possibility that different parameter values may be needed for the ocean case has not been addressed at all.

Here, we describe a study of turbulent fluxes in the upper equatorial ocean during a westerly windburst. This is a suitable regime for the quantification of nonlocal transports as it involves both vigorous convection and strong surface fluxes of heat, salt and momentum. We take advantage of the extensive and detailed observational database that resulted from TOGA-COARE (Webster and Lukas, 1992; Moum and Caldwell, 1994; Smyth et al., 1996a,b). Skillingstad et al. (1999) described large-eddy simulations (LES) of upper ocean mixing over a 24-hour period during a windburst using a model initialized with observed mean profiles and driven by observed surface fluxes. Statistical comparisons quantified the relationship between turbulent fluxes developed in the LES model and those inferred from *in situ* microstructure measurements. These comparisons establish the accuracy (and limits thereto) of the LES description of upper ocean turbulence, which is much more comprehensive than the view that the observations afford. Modeled turbulence statistics were shown to compare closely with observations in the mixed layer interior. Model performance was poorer in the stratified region below the mixed layer, wherein the energy containing scales of the turbulence contract to values smaller than the model’s spatial resolution.

Our plan here is to test the performance of the KPP model in this oceanic regime and suggest appropriate refinements. For this purpose, the KPP is incorporated into a one-dimensional model of the upper ocean, which is then initialized and forced using observations in the same manner as is the LES. Besides testing the KPP as a model for mixing in the windburst regime, we will derive values for the adjustable parameters needed to describe nonlocal fluxes of heat, salt and momentum in the upper ocean. In addition, we investigate two modifications to the KPP model that account for the effects of the Stokes drift, following suggestions of MS. First, the turbulent velocity scale is enhanced during stable conditions to account for

fluxes due to Langmuir cells. Second, the nonlocal momentum flux is supplemented by a term describing mixing of the Stokes drift velocity gradient.

We begin in section 2 with a discussion of our methodology. The LES methods and observational measurements are reviewed briefly, as is the overall structure of the KPP. Greater attention is given to methods for the parameterization of nonlocal fluxes and to the inclusion of penetrating solar radiation. Preliminary comparisons among observations, LES results, and results from the column model are described in section 4. This comparisons guide the more detailed analyses discussed later. Section 5 describes the essential results of the paper: modifications to the KPP that account for Stokes drift effects as well as revisions to the nonlocal flux parameterizations. Our main conclusions are summarized in section 6.

## 2 Observations

The R/V Moana Wave maintained station at  $1^{\circ}45'S, 156^{\circ}0'E$  from December 20th, 1992 to January 12th, 1993. Onboard meteorological measurements were processed using the TOGA COARE bulk flux algorithm (Fairall et al., 1996) to yield surface fluxes. Currents were measured using the shipboard Acoustic Doppler Current Profiler in combination with data from a nearby mooring (Weller and Anderson, 1996). Temperature, conductivity, and shear microstructure were measured using the Chameleon microstructure profiler (Moum et al., 1995).

The 24-hour period selected for analysis began at 00:00 UTC on December 31st, 1992. This period began in local midafternoon. Cloud cover was minimal, and winds were strong and steady from the west (figure 1a). A squall at  $t = 2$  hours interrupted the surface warming. The evening reversal of the surface heat flux led to convective conditions in the upper ocean and a rapid deepening of the mixed layer (figure 1b). Upper ocean current structure was dominated by the wave response to the windburst and by the semidiurnal tide (Smyth et al., 1996a). Thermal evolution during this period was controlled mainly by the local surface heat flux, while salinity increased in response to advection (Smyth et al., 1996b; Feng et al., 1998). The morning reversal of the heat flux was delayed by a second rain squall. Rain effects during this period are described more fully in Smyth et al. (1997).

Note that, despite complex time dependence, the velocity and salinity fields (shown in the first, second and fourth frames of figure 1b) are dominated by nearly vertical isolines in the upper 60m, suggesting that these fields are generally well mixed in this near-surface regime. The temperature field (third frame of figure 1b) exhibits stable stratification during the first few hours of the observation (the daytime portion), consistent with solar heating. Once the evening deepening of the mixed layer is complete, the temperature stratification in the upper 60m is reversed, with the highest temperatures occurring around 50-60m depth and colder water evident at the surface, as is typical in strongly convective conditions (e.g. Anis and Moum, 1992).

## 3 Models

### 3.1 The LES model

Our large-eddy modeling methods are described in detail in Skillingstad et al. (1999) and Skillingstad et al. (2000) and thus will only be summarized here. The computational domain is a 96m deep layer adjacent to the ocean surface, with lateral size 384m x 384m. The domain is periodic in both lateral directions. A radiation boundary condition is applied at the model bottom, and surface fluxes provide the upper boundary conditions. Surface wave effects are incorporated using the Stokes vortex force, with wave parameters based on observations. Subgrid scale (SGS) fluxes are parameterized using the filtered structure function method of Ducros et al. (1996). Spatial derivatives are discretized using second-order finite differences in flux form on a staggered C-grid, with spacing 1.5 m in all three coordinates. Time stepping is via the third-order Adams-Bashforth method. As in Skillingstad et al. (1999), the simulation was initialized using measured profiles of velocity, temperature and salinity, and forced subsequently by the observed surface fluxes described above. Simulations described here were performed on a 32 processor IBM SP-3.

### 3.2 The column model

The column model employed here solves the following equations for the zonal velocity  $U(z, t)$ , the meridional velocity  $V(z, t)$ , the temperature  $T(z, t)$  and the salinity

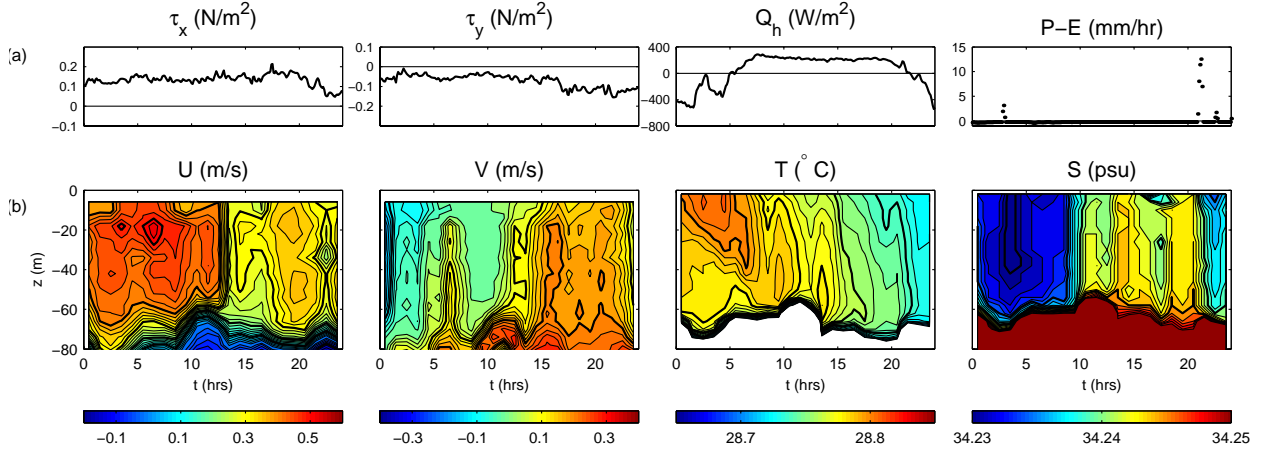


Figure 1: COARE observations. (a) Wind stresses, net surface heat flux and net precipitation rate observed at 156E, -1.75S for the 24-hour period beginning on day 366 of 1992. (b) Time-depth sections of zonal current, meridional current, temperature and salinity.

$S(z, t)$ :

$$\frac{\partial U}{\partial t} = -\frac{\partial}{\partial z} \overline{u'w'} + fV; \quad (1)$$

$$\frac{\partial V}{\partial t} = -\frac{\partial}{\partial z} \overline{v'w'} - fU; \quad (2)$$

$$\frac{\partial T}{\partial t} = -\frac{\partial}{\partial z} \overline{T'w'} - \frac{1}{\rho_o C_p} \frac{\partial Q_r}{\partial z}; \quad (3)$$

$$\frac{\partial S}{\partial t} = -\frac{\partial}{\partial z} \overline{S'w'}; \quad (4)$$

where  $z$  and  $t$  represent the vertical coordinate and time, respectively,  $f$  is the Coriolis parameter and  $Q_r(z, t)$  is a specified function representing the radiative heat flux. The mean density is approximated by  $\rho_o = 1030 \text{ kg m}^{-3}$ , and the specific heat capacity of water is  $C_p = 4000 \text{ J kg}^{-1} \text{ K}^{-1}$ . The fluxes  $\overline{x'w'}(z, t)$  (where  $x$  stands for any of  $u, v, T$  and  $S$  and primes represent turbulent fluctuations) are determined using the nonlocal K-profile parameterization described below. Initial conditions are provided by specified functions  $U(z, 0)$ ,  $V(z, 0)$ ,  $T(z, 0)$  and  $S(z, 0)$ . Time-dependent values of the surface fluxes  $\overline{x'w'}(0, t)$  are specified, while all fluxes are assumed to vanish at the lower domain boundary:  $\overline{x'w'}(-D, t) = 0$ . In the present application, the initial profiles and the fluxes at the upper boundary are provided by observational data and are identical to those used in the LES (section 3.1).

The vertical discretization is staggered, with fluxes being computed at a set of equally-spaced depths that include the upper and lower boundaries, and all prognostic variables defined on the intermediate points. Vertical derivatives are represented as second-order centered differences. The local components of the fluxes (see below) are advanced implicitly using the second-order Crank-Nicolson scheme, as is the radiative heat flux. The nonlocal fluxes, as well as the Coriolis terms, are advanced explicitly using the second-order Adams-Bashforth method.

The parameterization for the turbulent fluxes that appear in (1-4) has been described in detail by LMD. Here, we summarize the features that are most pertinent to the present experiments and describe the addition of the nonlocal momentum fluxes and Stokes drift effects. The parameterization requires separating the water column into two regions, the boundary layer and the underlying thermocline, which are separated by the surface  $z = -h(t)$ . The boundary layer depth  $h(t)$  is defined as the shallowest depth at which the bulk Richardson number,  $Ri_b(z, t)$ , exceeds a specified critical value  $Ri_c$ . The bulk Richardson number is defined by

$$Ri_b = \frac{B_{sl} - B}{|\vec{U}_{sl} - \vec{U}|^2 + V_t^2} (z_{sl} - z) \quad (5)$$

The buoyancy  $B(z, t)$  is given by  $-g\rho(z, t)/\rho_o$ , where

$g = 9.81 \text{ m s}^{-2}$  is the gravitational acceleration and  $\rho(z, t)$  is the density (obtained as a function of  $T$  and  $S$  using a standard equation of state for seawater).  $\vec{U}(z, t)$  is the horizontal velocity vector ( $U, V$ ). The subscript  $sl$  indicates values averaged over the surface layer, which is taken to be the upper one-tenth of the boundary layer, i.e.  $-0.1h < z < 0$ . In practice, the surface layer depth is computed using an initial guess at  $h$ , usually obtained as the value at the previous time step. The computation may be iterated if the time step is too large to resolve fluctuations in boundary layer depth accurately. In the present application, iteration is not required.  $V_t$  is a turbulent velocity magnitude described in detail in LMD (their equation 23). We will not repeat LMD's description except to note that  $V_t^2$  is proportional to a constant parameter  $C_v$ , whose value will be of interest to us here.

Each of the fluxes  $\overline{x'w'}$  that appear in (1-4) is expressed as a local and a nonlocal part, viz:

$$\overline{x'w'} = \overline{x'w'}_L + \overline{x'w'}_N, \quad (6)$$

The local component is given by the usual gradient parameterization

$$\overline{x'w'}_L = -K_x \frac{\partial X}{\partial z}, \quad (7)$$

where  $K_x(z, t)$  is the turbulent diffusivity and  $X(z, t)$  represents any of  $U, V, T$  and  $S$ . Parameterization of  $K_x$  is discussed in the remainder of this subsection; nonlocal fluxes are discussed in detail in subsection 3.3.

Below the boundary layer ( $z < -h$ ), fluxes are entirely local and are defined using a simple parameterization based on the gradient Richardson number,  $Ri = \frac{\partial B}{\partial z} / |\frac{\partial \vec{U}}{\partial z}|^2$ , viz:

$$K_x = \nu_x^w + \nu^o \begin{cases} 1 & Ri < 0 \\ (1 - Ri^2/Ri_0^2)^3 & 0 < Ri < Ri_0 \\ 0 & Ri > Ri_0 \end{cases} \quad (8)$$

The first term approximates diffusivity due to internal wave breaking, and takes the constant values  $\nu_m^w = 1.0 \times 10^{-4} \text{ m}^2 \text{ s}^{-1}$  for momentum and  $\nu_s^w = 1.0 \times 10^{-5} \text{ m}^2 \text{ s}^{-1}$  for scalars. The second term parameterizes diffusivity due to shear instability in regions of low  $Ri$ . The constant  $\nu^o$  has the value  $5 \times 10^{-3} \text{ m}^2 \text{ s}^{-1}$ . The cutoff value for the gradient Richardson number,  $Ri_0$ , was set to 0.7 by LMD. Large and Gent (1999) suggested that  $Ri_0$  be increased to 0.8. However, results presented here motivate retention of the smaller value.

Within the boundary layer ( $z > -h$ ), the diffusivity  $K_x$  is parameterized by

$$K_x(z, t) = h(t)w_x(z, t)G_x(z, t), \quad (9)$$

in which  $w_x$  is a turbulent velocity scale and  $G_x$  is a shape function. The velocity scales are given by

$$w_x(z, t) = \frac{\kappa u_*(t)}{\phi_x(z, t)}, \quad (10)$$

where  $\kappa = 0.4$  is the von Karman constant and  $u_*$  is the surface friction velocity. The structure function  $\phi_x$  is defined as a function of the scaled depth  $\zeta = z/L$ , where  $L$  is the Monin-Obukhov length scale (see LMD equations B1 and B2 for details). Continuity of fluxes requires that near-surface gradients obey the similarity scaling

$$\frac{\partial X}{\partial z} = -\frac{\overline{x'w'_0} \phi_x(\zeta)}{u_* \kappa |z|}, \quad (11)$$

where  $\overline{x'w'_0}$  is the surface flux of  $x$  (positive upwards). In unstable conditions,  $\phi$  is restricted so that it cannot exceed its value at the base of the surface layer. The shape function  $G_x$  is a cubic polynomial in  $\zeta$  whose four coefficients are determined by four matching conditions: at the surface  $G_x = 0$  and  $\partial G_x / \partial \zeta = 1$ , and at  $z = -h$  both the diffusivity  $K_x$  and its first derivative must be continuous with the values determined below the boundary layer by the Richardson number parameterization.

MS have suggested that extra mixing due to Langmuir circulations be accounted for by multiplying the turbulent velocity scale  $w_x$  by a factor  $(1 + C_w/La^4)^{1/2}$ , where  $La$  is the Langmuir number, given by  $La = (u_*/U_s)^{1/2}$ , and  $U_s$  is the Stokes drift velocity. This adjustment of the KPP model results in turbulent velocities proportional to  $U_s$  in the regime of small  $La$ , a known property of Langmuir turbulence. The constant  $C_w$  was given the value 0.08 on the basis of fits to large eddy simulations of quasi-stationary, weakly convecting Langmuir turbulence. MS also suggested that this parameterization may require modification in regimes of either strong convection or strong wind forcing, both of which occur here. Accordingly, we multiply  $C_w$  by an additional factor that enhances the effect of Langmuir cells in stable (wind-forced) conditions and reduces it in convective conditions:

$$w_x(z, t) = \frac{\kappa u_*(t)}{\phi_x(z, t)} \times \left\{ 1 + \frac{C_w(u_*, w_*)}{La^4} \right\}^{1/2}, \quad (12)$$

in which

$$C_w(u_*, w_*) = C_{wo} \left[ \frac{u_*^3}{u_*^3 + 0.6w_*^3} \right]^l, \quad (13)$$

$w_*$  is the convective velocity scale (defined following LMD as  $w_*^3 = \kappa B_f h$ , where  $B_f$  is the surface buoyancy flux), and  $C_{wo}$  and  $l$  are constants to be determined.

### 3.3 Nonlocal fluxes in the KPP

The nonlocal flux of the property  $x$  is the flux due to eddies comparable in size to the scale on which the background gradient  $\partial X/\partial z$  varies. Nonlocal fluxes may be written in terms of local variables by making various approximations to the flux budget (e.g. Deardorff, 1972; Therry and Lacarrere, 1983; Holtzag and Moeng, 1991). In low-order closure models, however, those fluxes must be parameterized in terms of resolved variables. Typically, the parameterization is contained within an effective ‘‘gradient’’,  $-\gamma_x(z, t)$ , that is added to the background gradient, i.e.

$$\overline{x'w'_N} = K_x \gamma_x. \quad (14)$$

LMD deferred the implementation of nonlocal momentum fluxes due to lack of observational data for calibration, and instead concentrated on parameterizing nonlocal scalar fluxes via the effective gradient  $\gamma_s$ . They set  $\gamma_s$  to zero in stable conditions, but for convective conditions used the definition

$$\gamma_s(z, t) = C_s \frac{\overline{s'w'_0}(t)}{w_s(z, t)h(t)}, \quad (15)$$

where  $s$  represents any scalar concentration,  $\overline{s'w'_0}$  is the surface flux of  $s$  and  $w_s$  is the turbulent velocity scale for scalars. The constant  $C_s$  is written as  $C_s^* \kappa (c_s \kappa \epsilon)^{1/3}$ , in which  $c_s$  is an additional constant that appears in the structure function for convective conditions:  $\phi_s = (a_s - c_s \zeta)^{-1/3}$ .  $C_s^*$  is regarded as a universal constant. The constant  $\epsilon$  represents the depth of the surface layer as a fraction of the boundary layer depth, here equal to 0.1. In the original analyses of Deardorff (e.g. Deardorff, 1972), the constant  $C_s^*$  was expected to be of order 10. Mailhot and Benoit (1982) adopted this value for their atmospheric simulations and obtained acceptable results. An explicit attempt to determine the best value for  $C_s^*$  was carried out by Therry and Lacarrere (1983), who obtained optimal results using the value  $C_s^* = 5$ . The same result was found by Holtzag and Moeng (1991) on the basis of

comparisons with LES. In constructing the original KPP, LMD used Deardorff’s estimate,  $C_s^* = 10$ . Results described later in this paper suggest that the smaller value is preferable.

A similar parameterization can be devised for the nonlocal momentum flux. Following the atmospheric modeling work of Brown and Grant (1997) and Frech and Mahrt (1995), we write

$$\gamma_{\vec{u}}(z, t) = -C_m \frac{u_*^2}{w_m(z, t)h(t)} A(u_*, w_*) \hat{e}. \quad (16)$$

The constant  $C_m$  corresponds to  $S_m$  in Brown and Grant (1997) and Frech and Mahrt (1995), and is scaled as  $C_m^* \kappa (c_m \kappa \epsilon)^{1/3}$  analogously with the scalar case. The factor  $A(u_*, w_*)$  represents enhancement of the nonlocal flux in strongly unstable conditions. The unit vector  $\hat{e}$  defines the lateral direction of the flux.

Frech and Mahrt (1995) suggested that the stability function  $A(u_*, w_*)$  take the form

$$A(u_*, w_*) = 1 + w_*/u_* \quad (17)$$

In more recent atmospheric simulations, Brown and Grant (1997) have shown that this form exaggerates the nonlocal flux in neutral stratification, and suggested the alternative form

$$A(u_*, w_*) = 2.7w_*^3/(u_*^3 + 0.6w_*^3). \quad (18)$$

In our simulations of turbulence in the equatorial ocean, the expressions (17) and (18) for  $A$  are nearly proportional throughout the night (the second exceeds the first by a factor that varies between 1.22 and 1.25). However,  $A$  as defined by (18) vanishes during the day, a desirable property. We therefore adopt (18) as the stability function in the present work.

There is also uncertainty over the best representation of the direction vector,  $\hat{e}$ . Frech and Mahrt (1995) defined  $\hat{e}$  as the direction of the mean vertical shear of the horizontal current between the middle of the surface layer and the base of the boundary layer, i.e.  $\hat{e} = (\vec{U}_{sl} - \vec{U}_h)/|\vec{U}_{sl} - \vec{U}_h|$ . An alternative recommended by Brown and Grant (1997) is to have  $\hat{e}$  correspond to the direction of the wind. In the present equatorial regime, the Coriolis force is weak, so that the surface current remains nearly aligned with the wind. As a result, these two directions differ very little (by ten degrees or less during the night, when the nonlocal fluxes are active). For the present simulations, we retain the Frech & Mahrt definition.

A value must be chosen for the amplitude parameter,  $C_m$  or, equivalently, for  $C_m^*$ . Due to the lack of available data, LMD set  $C_m^*$  to zero. In comparisons of atmospheric boundary layer simulations with observations, Brown and Grant (1997) concluded that values of  $C_m$  up to 1.4 give reasonable results, while the preferred value is 0.8. In our notation,  $C_m = 0.8$  and 1.4 correspond to  $C_m^* = 2.3$  and 4.0, respectively.

Thus, available values for both  $C_m^*$  and  $C_s^*$  are based on atmospheric cases. A goal of the present paper is to provide values for these constants that are appropriate for the upper ocean boundary layer (sections 5.2 and 5.3). Finally, MS suggest that nonlocal momentum fluxes due to Langmuir cells be included in the model by adding the shear of the Stokes drift to  $\gamma_x$ . We will test that possibility in the present analyses (section 5.4).

### 3.4 The radiative heat flux

Heat balances in the upper ocean during COARE were strongly influenced by the heat flux due to the penetration of solar radiation to significant depths beneath the sea surface (Weller and Anderson, 1996; Smyth et al., 1996b; Ohlmann et al., 1998). Here, we parameterize the radiative heat flux as

$$Q_r(z, t) = E_d(t)Tr(z, t), \quad (19)$$

in which  $E_d$  is the downwelling radiation measured just above the sea surface and  $Tr$  is the transmission function.  $E_d(t)$  was measured locally (Fairall et al., 1996), and the transmission function was measured aboard a nearby vessel (Siegel et al., 1995; Ohlmann et al., 1998). Measured profiles of  $Tr(z, t)$  were fitted to a two-term exponential decay representation:

$$Tr = r_1 e^{z/\mu_1} + r_2 e^{z/\mu_2} \quad (20)$$

using a nonlinear least-squares method (figure 2). [A four-term expansion model has recently been developed by Ohlmann and Siegel (2000). This enhanced model captures the rapid attenuation in the upper meter of the water column. For the present application, the shallowest point at which the flux is needed is typically 1m, so the two-term expansion described above is sufficient.] Because the measurements were not made at exactly the same coordinates, we accounted for possible spatial variations by averaging profiles from days 365, 366 and 367, with double weight given to day 366. The result was

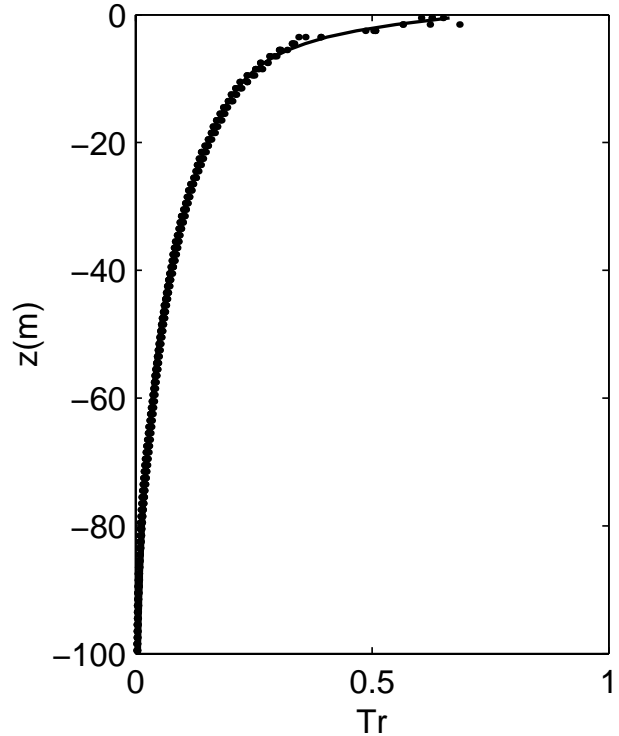


Figure 2: Solar radiation transmissivity as a function of depth. Dots show daily averages from days 365, 366 and 367 as measured by Siegel et al. (1995). The solid curve represents the approximation (20), with parameter values as given in the text.

$r_1 = 0.316; r_2 = 0.419; \mu_1 = 27.2m; \mu_2 = 2.93m$ . By definition,  $Tr(0) = 1 - \alpha$ , where  $\alpha$  is the albedo, here equal to 0.055 (Fairall et al., 1996). The fact that  $r_1 + r_2 < 1 - \alpha$  indicates that significant radiation is absorbed between the surface and the uppermost measurement, located at  $z = -0.5m$  (Ohlmann and Siegel, 2000). Thus, we use (20) at all grid points except at the surface, where  $Tr(0) = 0.945$ .

## 4 Preliminary comparisons

The LES results for this period (figure 3b) are very similar to those described in Skyllingstad et al. (1999), although several minor upgrades have been made to the model in the interim (see section 3.1). Momentum input from the

wind is mixed through the upper ocean with only weak influence from the Coriolis force. Because no attempt has been made to include tidal effects or large-scale gradients in the LES model, the complex time dependence of the observed near-surface currents is not evident (compare figures 1b and 3b, first and second frames). However, the nocturnal upper ocean exhibits a well-mixed velocity structure consistent with the observations. The modeled thermal evolution is quite similar to observations, although there is slightly more daytime heating and less night-time cooling. This discrepancy is consistent with the slight advective cooling that emerged in the observational analyses of Smyth et al. (1996b) and Feng et al. (1998). Thermal stratification in the modeled nocturnal mixed layer is nearly neutral, as shown by the nearly vertical isotherms in frame 3 of figure 3b. Salinity (fourth frame of figure 3b) increases over most of the analysis period due to evaporation, though freshening due to rain is evident at  $t = 2$  hrs and during the last few hours of the simulation. Like the temperature field, the nocturnal salinity field is well-mixed near the surface, though it exhibits significant stratification between 50 and 60m that is not evident in the temperature.

Figures 3c and 3d show results from two versions the KPP column model, initialized and forced in the same manner as the LES. The model used to generate figure 3c approximates turbulent fluxes in accordance with the original KPP rules of LMD, while figure 3d corresponds to a revised version of the KPP to be described later in this paper. To motivate the latter, we now compare the results of the original KPP model (figure 3c) with the LES (figure 3b). Three important differences are evident.

1. Most obviously, both velocity components exhibit significant gradients within the nocturnal mixed layer in the KPP case, as do the temperature and the salinity. The temperature gradient in this regime is not only nonzero but positive, opposite to the observed gradient (cf. figures 3c and 1b, third frame).
2. Upper ocean heating during the first few hours of the simulation is much more pronounced in the KPP case than in the LES.
3. Near surface shear is stronger in the KPP than in the LES throughout the simulation period.

In section 5, we will describe these discrepancies quantitatively and seek to reduce them via revisions to the KPP model. We will use the LES results as a standard against

which to test and calibrate our revisions. Our confidence in the LES as the appropriate “ground truth” for this exercise is based on several factors. First, while the LES does not contain the entirety of upper ocean physics, it contains that part which the KPP attempts to model, namely vertical fluxes due to turbulence, and it represents the large turbulent eddies that drive those fluxes explicitly. This particular LES model has been tested via comparison with microstructure measurements, and has been found to reproduce the observed statistics of turbulence extremely well within well-established limits (Skylningstad et al., 1999). Finally, we can investigate the specific discrepancies between the KPP and the LES listed above while also considering the implications of the observational data for the veracity of the LES results. Like the LES, the observations show no sign of the strong gradients in  $U$ ,  $V$ ,  $T$  and  $S$  developed by the KPP in the interior of the nocturnal mixed layer (figure 1b). Daytime heating is even weaker in the observations than in the LES, though this difference is exaggerated by advective cooling. Finally, the observations show no evidence of the strong shears developed by the KPP in the upper few meters, though this could also be due to observational uncertainties. Although these comparisons are not conclusive, the weight of evidence suggests that the LES results provide a reasonable standard against which to test the KPP model.

## 5 Modifications to the KPP

After considerable experimentation, we have identified several modifications to the KPP that appear to be of general utility. In this section, we describe these revisions in roughly the chronological order in which they become important in the present simulations. We begin with enhanced mixing due to Langmuir cells, which modulates near-surface warming during the first six hours of the simulation period. We then describe the nonlocal fluxes of momentum and scalars, which determine vertical gradients in the nocturnal mixed layer. Finally, we show that unrealistically strong shears in the upper few meters may be controlled by including shear due to the Stokes drift in the momentum mixing term.



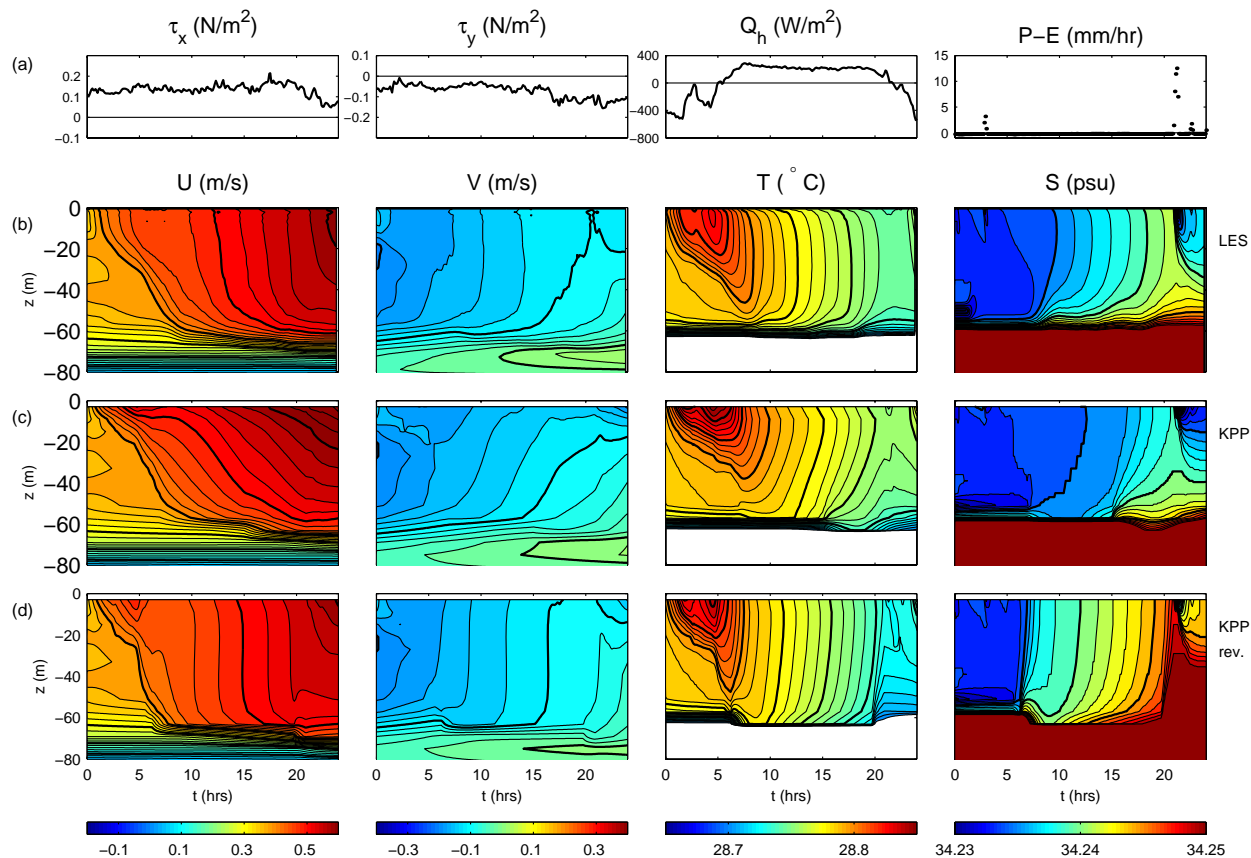


Figure 3: Model results. (a) Wind stresses, net surface heat flux and net precipitation rate observed at 156E, -1.75S for the 24-hour period beginning on day 366 of 1992. (b,c,d) Time-depth sections of zonal current, meridional current, temperature and salinity. (b) LES; (c) original KPP; (d) revised KPP.

### 5.1 Amplification of wind-driven mixing by Langmuir cells

The moderate daytime warming in the LES is largely a result of Langmuir cells, which distribute solar heat over the upper few tens of meters. This effect is missing from the existing KPP model, with the result that upper ocean temperatures (averaged over the uppermost 10m) increased by  $0.02^\circ C$  more in the KPP than in the LES (figure 4, solid curves). Attempts to produce sufficient near-surface mixing in the KPP by varying the values of existing parameters by reasonable amounts have not been successful.

MS suggest a parameterization in terms of Langmuir number (see section 3.2), which effectively boosts the tur-

bulent velocity scales  $w_m$  and  $w_s$  by about a factor of three for the present case. This leads to reduced daytime warming near the surface, in qualitative agreement with LES (figure 4, asterisks). However, the reduction in daytime warming is insufficient to reproduce the LES results quantitatively, while application of the parameterization during nocturnal convection causes unrealistically rapid mixing throughout the mixed layer.

The Langmuir cell parameterization shown in figure 4 was calibrated for weakly stable conditions. Evidently, the scheme mixes too weakly in strongly stable conditions ( $0 < t < 6hrs.$ ) and too strongly in the unstable conditions. We therefore make the amplitude parameter  $C_w$  a function of stability using (13). We now have two free pa-

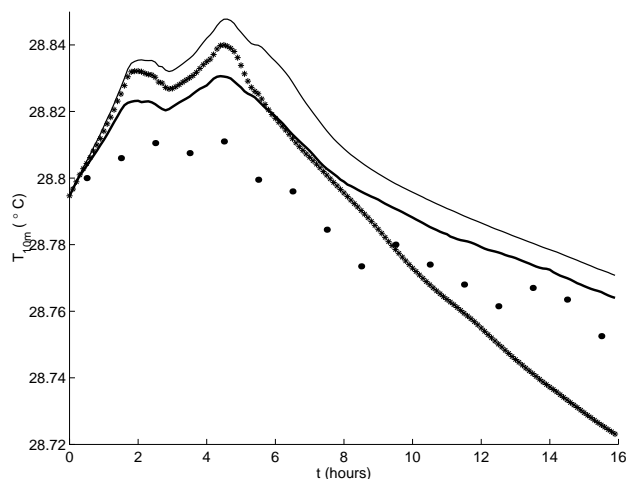


Figure 4: Temperature averaged over the upper 10m. Dots: observations. Thick curve: LES. Thin curve: original KPP. Asterisks: KPP with MS parameterization of mixing due to Langmuir cells ( $C_{wo} = 0.08, l = 0$ ).

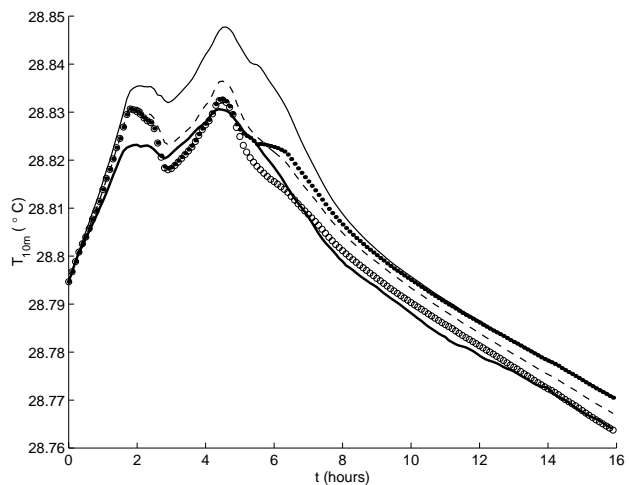


Figure 5: Temperature averaged over the upper 10m. Thick curve: LES. Thin curve: original KPP. Dashed curve: KPP with MS parameterization of mixing due to Langmuir cells, but  $C_{wo} = 0.15, l = 2$ . Dotted curve:  $C_{wo} = 0.29, l = 4$ . Circles:  $C_{wo} = 0.29, l = 2$ .

rameters,  $C_{wo}$  and  $l$ , to calibrate. The MS results provide one data point, which we fit to (13) to infer the relation  $C_{wo} = 0.08/0.726^l$ . Figure 5 shows upper ocean warming for two additional choices of  $C_{wo}$  and  $l$  that obey this relation, and one that does not (along with the original KPP and “target” LES results).

The choice  $C_{wo} = 0.15, l = 2$  (dashed curve on figure 5) provides a much improved fit to the LES, although it mixes too weakly (i.e. allows too much heating in the upper 10m) throughout the simulation. More extreme stability dependence is provided by the case  $C_{wo} = 0.29, l = 4$  (dots). In this case, the Langmuir cell effect ceases abruptly as the surface fluxes become stable. The result is reduced near-surface mixing in the early evening. The final case shown is  $C_{wo} = 0.29, l = 2$  (circles), which provides the best overall fit to our LES results. However, this is the case that does not obey the constraint  $C_{wo} = 0.08/0.726^l$ , i.e. it would not provide a good fit to the MS results.

For the remaining analyses, we make the conservative choice  $C_{wo} = 0.15, l = 2$ . This choice provides enough extra mixing in stable conditions to greatly ameliorate the problem of excessive daytime heating, does not lead to excessive mixing at night, and reproduces the MS result  $C_w = 0.08$  for the appropriate values of  $u_*$  and  $w_*$ .

## 5.2 Nonlocal momentum flux

The amplitude parameter  $C_m^*$  for the nonlocal momentum flux has been set to zero in previous versions of the KPP rules. Here, we assign a nonzero value to that parameter in order to reduce the shear in the nocturnal mixed layer from the large value seen in figure 3c to a level more consistent with the LES and observed values.

To make this comparison quantitative, we compute the arithmetic mean of the zonal shear  $\partial U/\partial z$  in the regime  $-40\text{m} < z < -20\text{m}$ ;  $11\text{hrs} < t < 20\text{hrs}$ , which represents the interior of the nocturnal mixed layer. Also of interest is the zonal acceleration over the same depth-time range. These parameters are shown as functions of  $C_m^*$  in figure 6. As anticipated, the mean shear decreases as  $C_m^*$  increases from zero (figure 6a), and reaches zero when  $C_m^* = 5.2$ . The LES mean shear is best reproduced using the value  $C_m^* = 3.3$ . The optimal value of Brown and Grant (1997),  $C_m^* = 2.3$ , yields a mean shear part-way between the LES value and the observed value. For the remaining analyses, we choose the intermediate value  $C_m^* = 3.0$ .

The acceleration is slightly greater than the LES value (figure 6b), and does not vary significantly with  $C_m^*$ . Also

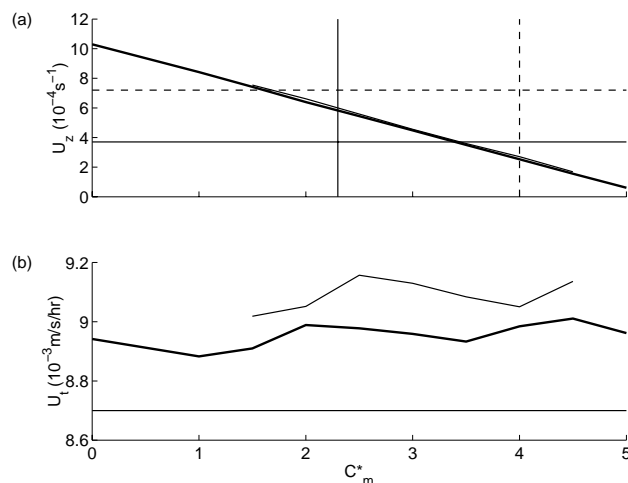


Figure 6: Zonal shear and acceleration, averaged over  $-40\text{m} < z < -20\text{m}$ ;  $11\text{hrs} < t < 20\text{hrs}$ , as functions of the nonlocal momentum flux amplitude parameter  $C_m^*$ . Thick curve:  $C_s^* = 10$ ,  $C_v = 1.5$  (original KPP values). Thin curve:  $C_s^* = 5$ ,  $C_v = 1.0$  (revised values to be discussed in section 5.3). (a) Shear. Horizontal lines: solid = LES shear, dashed = observed shear. Vertical lines indicate values derived by Brown and Grant (1997) from atmospheric simulations: solid = optimal value, dashed = maximum value. (b) Acceleration. Horizontal line = LES acceleration. (Observed acceleration is not shown because it is dominated by tides.)

shown in figure 6 are results for a new set of values for the parameters  $C_s^*$  and  $C_v$ , whose derivation is described in the next subsection. Note for now that these revised values for  $C_s^*$  and  $C_v$  have a minimal effect on the zonal shear and acceleration in the nocturnal boundary layer and therefore do not affect the optimal choice of  $C_m^*$ .

Figure 7 shows profiles of the vertical flux of zonal momentum in the nocturnal boundary layer. Flux profiles are averaged over a 9 hour period during which mixed layer depth was nearly stationary and vigorous convective turbulence was driven by surface cooling. In the original KPP (figure 7b), the flux is entirely local and is slightly stronger than in the LES results (figure 7a). In the revised KPP case, the net flux is nearly identical to that found in the original KPP, but that flux is now composed of local and nonlocal components whose overall magnitude is comparable.

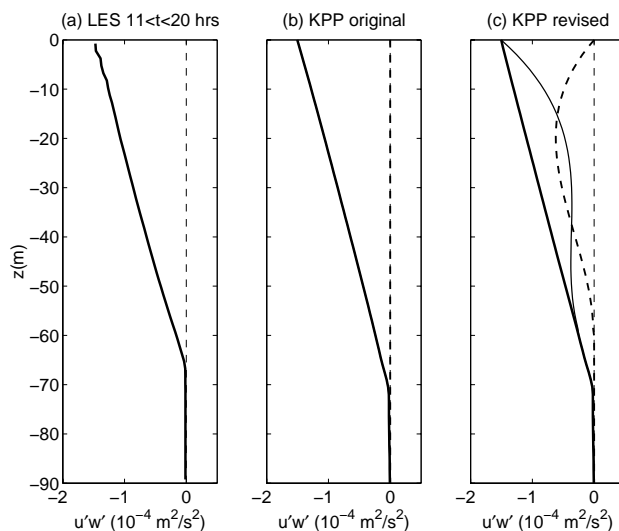


Figure 7: Vertical flux of zonal momentum versus depth, averaged over  $11\text{hrs} < t < 20\text{hrs}$ . (a) LES. (b) Original KPP. (c) Revised KPP. Thick solid curves: total flux; thin solid curves: local flux; thick dashed curves: nonlocal flux; thin dashed lines: zero flux.

### 5.3 Nonlocal scalar fluxes

The amplitude parameter  $C_s^*$  for the nonlocal scalar flux has been set to 10 in previous versions of the KPP rules, based on the original estimates of Deardorff (1972) and the simulations of Mailhot and Benoit (1982). Calibrations by Therry and Lacarrere (1983) and Holtzlag and Moeng (1991) have suggested the smaller value  $C_s^* = 5$ . In this subsection, we show that using the smaller value of  $C_s^*$  reduces the scalar gradients in the nocturnal mixed layer to more realistic values. However, the reduction of  $C_s^*$  necessitates compensating changes in other parameters.

Figure 8a shows the vertical temperature gradient averaged over the nocturnal mixed layer as a function of  $C_s^*$ . The LES value of the temperature gradient (horizontal line) is recovered when  $C_s^*$  is slightly greater than 4. Figure 8b shows  $\beta_T$ , the heat flux into the mixed layer due to entrainment at the mixed layer base, scaled by the surface heat flux. All versions of the KPP give values of  $\beta_T$  more negative than the LES result, indicating that the KPP develops a stronger entrainment flux. Correspondingly, the cooling rate in the nocturnal mixed layer (figure

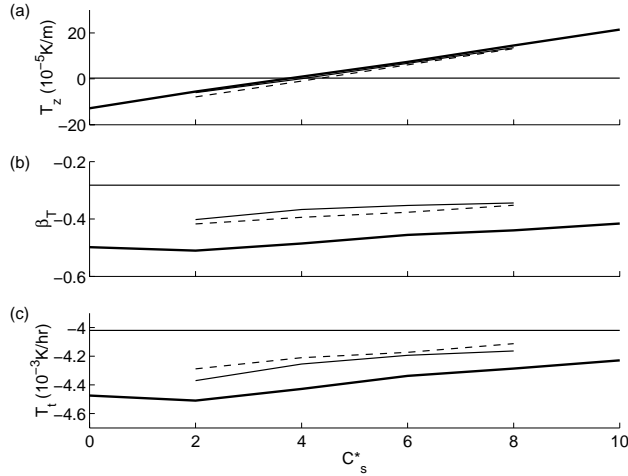


Figure 8: (a) Vertical derivative of temperature, averaged over  $-40\text{m} < z < -20\text{m}$ ;  $11\text{hrs} < t < 20\text{hrs}$ , as a function of the nonlocal scalar flux amplitude parameter  $C_s^*$ , with  $C_m = 3$ . (b) Ratio of the minimum (negative) heat flux in the entrainment zone to the (positive) surface heat flux, averaged over  $11\text{hrs} < t < 20\text{hrs}$ . (c) Time derivative of temperature, averaged over  $-40\text{m} < z < -20\text{m}$ ;  $11\text{hrs} < t < 20\text{hrs}$ . Thick curves:  $Ri_o = 0.7, C_v = 1.5$  (original KPP values). Thin curves:  $Ri_o = 0.5, C_v = 1.5$ . Dashed curves:  $Ri_o = 0.7, C_v = 1.0$ . Solid horizontal lines indicate the LES values.

8c) is slightly faster for the KPP cases than for the LES. This discrepancy is exacerbated by the reduction of  $C_s^*$  from its original value of 10.

Our intent now is to identify other parameters whose values may be altered in order to remove this undesirable increase in entrainment due to the reduction in the nonlocal scalar fluxes. We do not attempt to match the LES results in this respect; our goal is only to recover the smaller mismatch delivered by the original KPP parameter values. After some experimentation, we have found two reasonable candidate parameters. The first is  $Ri_o$ , the cutoff value for the Richardson number in the parameterization (8) of turbulence below the boundary layer. The result of reducing  $Ri_o$  from its original value of 0.7 to 0.5 is shown by the thin solid curves in figure 8. The second possibility is to reduce the value of  $C_v$ , effectively reducing the turbulent velocity parameter  $V_t$  that appears in the bulk Richardson number used to determine boundary layer depth. The results of reducing  $C_v$  from 1.5 to 1.0 are

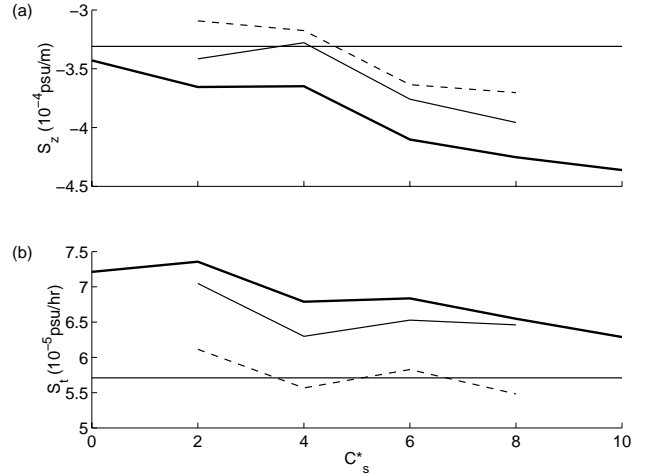


Figure 9: (a) Vertical derivative of salinity, averaged over  $-40\text{m} < z < -20\text{m}$ ;  $11\text{hrs} < t < 20\text{hrs}$ , as a function of the nonlocal scalar flux amplitude parameter  $C_s^*$ , with  $C_m = 3$ . (b) Time derivative of salinity, averaged over the same regime. Thick curves:  $Ri_o = 0.7, C_v = 1.5$  (original KPP values). Thin curves:  $Ri_o = 0.5, C_v = 1.5$ . Dashed curves:  $Ri_o = 0.7, C_v = 1.0$ . Horizontal lines indicate the LES values.

shown by the dashed curves in figure 8. The values of  $Ri_o$  and  $C_v$  have little effect on the mean temperature gradients shown in figure 8a. However, both of these changes compensate effectively for the reduction in the value of  $C_s^*$ , reducing the rate of entrainment into the mixed layer to below the value found in the original KPP (though the entrainment rate remains higher than in the LES results).

Similar results are found via analysis of the salinity field (figure 9). Reduction of  $C_s^*$  from 10 reduces the vertical salinity gradient in the nocturnal mixed layer from the unrealistically large value delivered by the original KPP to a smaller value consistent with the LES results (figure 9a). As with temperature, this change results in increased entrainment at the mixed layer base, and thus in a more rapid increase in mixed layer salinity (figure 9b). Setting  $Ri_o$  to 0.5 reduces salt entrainment nearly to the rate delivered by the original KPP (the value of the thick, solid curve at  $C_s^* = 10$ ), while reduction of  $C_v$  to 1.0 reduces entrainment to a rate consistent with the LES results (horizontal solid line).

Results presented so far give no compelling reason to choose between  $Ri_o$  and  $C_v$  as the parameter whose value

should be reduced to compensate for the reduced nonlocal scalar flux. Reducing  $Ri_0$  acts to reduce mixing rates below the boundary layer, whereas reducing  $C_v$  tends to make the boundary layer slightly shallower. Since the boundary layer generated by the KPP is already too deep (figure 7), we choose the second alternative. For the remainder of this discussion, we will set  $C_s$  to 5.0 and  $C_v$  to 1.0, leaving  $Ri_0$  at its original value 0.7.

Our changes to the values of  $C_s^*$  and  $C_v$  raise the possibility that the optimal value for  $C_m^*$  calculated in section 5.2 is no longer optimal. This turns out not to be the case. Results shown in figure 6 change only slightly when the revised values of  $C_s^*$  and  $C_v$  are employed (thin, solid curves on figure 6), and the arguments for our choice  $C_m^* = 3$  are unaffected.

## 5.4 Mixing of the Stokes drift velocity profile

As noted in section 4, the KPP tends to produce strong near-surface shears relative to LES. In the LES, these shears are prevented by strong, small-scale Langmuir cells in the upper few meters. The corresponding mixing can be achieved in the KPP by adding strong momentum mixing near the surface. MS suggest that the effective velocity gradient that controls the nonlocal momentum flux be supplemented with the shear of the Stokes drift current. The latter is given by

$$\vec{u}_s(z) = U_s e^{\mu z} \hat{e} \quad (21)$$

where  $U_s$  is the maximum Stokes drift velocity, determined by wave height and equal to  $11.5u_*$  in the present LES. The unit vector  $\hat{e}$  points in the direction of the wind, and the vertical decay rate  $\mu$  is equal to  $2\pi/\lambda$  where  $\lambda$  is the dominant wavelength of the surface wave field, here equal to  $30m$ .

Figure 10 shows the zonal and meridional velocity components, averaged over the analysis period. Cases shown include the LES along with the KPP with  $\partial\vec{u}_s/\partial z$  added to  $\partial\vec{U}/\partial z$  in the parameterization (7) of the vertical momentum flux in various proportions (quantified by  $C_{St}$ ). The LES velocity profiles (thick curves on figure 10) exhibit very little shear in the upper 10m. In contrast, the original KPP profiles (thin curves) are strongly sheared. When revised to take account of amplified mixing due to Langmuir cells (section 5.1), nonlocal momentum fluxes (section 5.2) and reduced nonlocal scalar

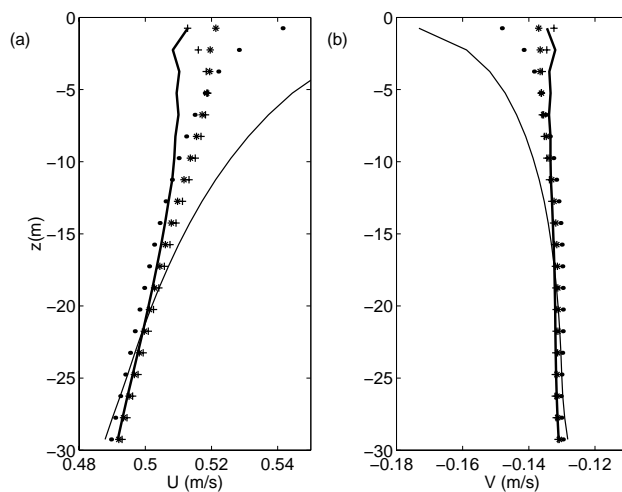


Figure 10: Zonal (a) and meridional (b) velocity components in the upper 30m, averaged over the 24-hour run. Thick, solid curve: LES. Thin, solid curve: original KPP. Dots, KPP with  $C_{St} = 0$ . Plusses, KPP with  $C_{St} = 1$ . Asterisks, KPP with  $C_{St} = 0.7$ .

fluxes compensated by reduction of  $C_v$  (section 5.3), the KPP model exhibits strong shear only in the upper 5m (dots on figure 10). When the shear of the Stokes drift is added to the nonlocal momentum flux as described above, shear is reduced further, to the point of slight overcompensation (plusses on figure 10). The asterisks on figure 10 show an intermediate case in which 70% of the Stokes drift shear has been added to the nonlocal flux. This provides the best match to the LES velocity profile.

Complete fields delivered by this model are shown in figure 3d. Vertical gradients of the velocity, temperature and salinity in the nocturnal mixed layer now correspond well with LES results (figure 3b), in contrast with the original KPP results (figure 3c). Solar heating during the first few hours of the simulation now agrees with the LES results, and the anomalous current shears that the original KPP developed in the upper 10m have been effectively removed.

## 6 Conclusions

We have tested and revised the KPP model using observations and LES of the upper equatorial Pacific during a

Westerly windburst. Four revisions have been made to the existing KPP:

1. The turbulent velocity scales have been amplified to account for mixing by Langmuir cells using (12). The effect is reduced during unstable conditions using (13), with  $C_{wo} = 0.15$  and  $l = 2$ . These parameter values were arrived at by requiring that daytime solar heat input be mixed at a rate consistent with LES, and are consistent with the parameterization suggested by MS.
2. A nonlocal momentum flux was added in accordance with (16). Stability dependence was provided using (18), and the flux was directed parallel to the wind. The amplitude parameter  $C_m^*$  was set to 3.0 by requiring that the mean zonal shear in the nocturnal mixed layer match the LES value.
3. The amplitude parameter for the nonlocal scalar flux was reduced from its original value  $C_s^* = 10$  to  $C_s^* = 5$  in order to obtain realistic scalar gradients in the nocturnal mixed layer. To compensate for excessive entrainment at the base of the mixed layer due to this change in  $C_s^*$ , we reduced the turbulent velocity parameter  $C_v$  to 1.0 from its original value 1.5.
4. Strong, near-surface shears appearing in the KPP results were removed by adding 0.7 times the shear of the Stokes drift current to the effective shear governing the nonlocal momentum flux.

The fourth change listed above is somewhat *ad hoc*; there is no particular reason why the shear of the Stokes drift should contribute to the momentum flux in this way. This artifice merely provides enhanced mixing near the surface with the correct properties to remove the strong near-surface shear developed by the KPP as a result of matching to a surface layer similarity solution (LMD). Such matching is probably inappropriate in the ocean due to the presence of surface waves. A more physical solution to this problem must await further progress in the parameterization of surface wave effects.

These changes led to much better agreement between the KPP results and the corresponding LES. By generating realistically small gradients in the nocturnal mixed layer, these changes will improve the representation of lateral advection in large-scale models that use KPP to model vertical mixing. Finally, increased mixing of solar

heat will improve predictions of sea-surface temperature, a crucial factor in coupled models.

Further development of the KPP rules will require testing against a wider range of observational datasets. Such tests must examine the generality of the nonlocal flux and Langmuir cell parameterizations used here. In particular, further testing must address three issues that have not been adequately resolved in the present work:

- The optimal choice of the direction vector  $\hat{e}$  for the nonlocal momentum flux should be identifiable in midlatitude regimes where surface currents are less likely to be aligned with the wind.
- Unwanted effects of reducing the value of the nonlocal scalar flux parameter  $C_s^*$  from 10 to 5 may be removed by reducing either  $C_v$  and  $Ri_0$  (or some combination of the two). Detailed examination mixing around the base of the boundary layer will allow us to make that choice with more confidence.
- Accounting for fluxes due to breaking surface waves remains a central goal in modeling upper ocean turbulence.

**Acknowledgements:** Optical transmissivity data were generously provided by Dave Siegel and Carter Ohlmann. Supercomputer time for the LES computations was provided by the National Center for Atmospheric Research. The research was funded by the National Science Foundation under grant OCE9711862.

## References

- Anis, A. and J. Moum, 1992: The superadiabatic surface layer of the ocean during convection. *J. Phys. Oceanogr.*, **22**, 1221–1227.
- Brown, A. and A. Grant, 1997: Non-local mixing of momentum in the convective boundary layer. *Boundary Layer Meteorology*, **84**, 1–22.
- Burchard, H., O. Petersen, and T. Rippeth, 1998: Comparing the performance of the Mellor-Yamada and the  $k-\epsilon$  two-equation turbulence models. *J. Geophys. Res.*, **103**, 10543–10554.

- Deardorff, J., 1972: Theoretical expression for the countergradient vertical heat flux. *J. Geophys. Res.*, **77**, 5900–5904.
- Ducros, F., P. Comte, and M. Lesieur, 1996: Large eddy simulation of transition to turbulence in a boundary layer developing spatially over a flat plate. *J. Fluid Mech.*, **326**, 1–36.
- Fairall, C., E. Bradley, D. Rogers, J. Edson, and G. Young, 1996: The TOGA-COARE bulk flux algorithm. *J. Geophys. Res.*, **101**, 3747–3764.
- Feng, M., P. Hacker, and R. Lukas, 1998: Upper ocean heat and salt balances in response to a westerly wind burst in the western equatorial Pacific during TOGA-COARE. *J. Geophys. Res.*, **103**, 10289–10311.
- Frech, M. and L. Mahrt, 1995: A two-scale mixing formulation for the atmospheric boundary layer. *Boundary Layer Meteorology*, **73**, 91–104.
- Holtzlag, A. and C.-H. Moeng, 1991: Eddy diffusivity and countergradient transport in the convective atmospheric boundary layer. *J. Atmos. Sci.*, **48**, 1690–1698.
- Kantha, L. and C. Clayson, 1994: An improved mixed layer model for geophysical applications. *J. Geophys. Res.*, **99**, 25235–25266.
- Large, W. and P. Gent, 1999: Validation of vertical mixing in an equatorial ocean model using large eddy simulations and observations. *J. Phys. Oceanogr.*, **29**, 449–464.
- Mailhot, J. and R. Benoit, 1982: A finite-element model of the atmospheric boundary layer suitable for use with numerical weather prediction models. *J. Atmos. Sci.*, **39**, 2249–2262.
- McWilliams, J. and P. Sullivan, 2001: Vertical mixing by Langmuir circulations. *Spill Sci. Technol. Bull.*, **6**, 225–237.
- Mellor, G. and T. Yamada, 1982: Development of a turbulence closure model for geophysical fluid problems. *Rev. Geophys. Space Phys.*, **20**, 851–875.
- Moum, J. and D. Caldwell, 1994: Experiment explores the dynamics of ocean mixing. *EOS Trans.*, **75**, 489–495.
- Moum, J. N., M. C. Gregg, R. C. Lien, and M. E. Carr, 1995: Comparison of turbulence kinetic energy dissipation rate estimates from two ocean microstructure profilers. *J. Atmos. Oceanic Technol.*, **12**(2), 346–366.
- Ohlmann, J. and D. Siegel, 2000: Ocean radiant heating. Part 2: Parameterizing solar radiation transmission through the upper ocean. *J. Phys. Oceanogr.*, **30**, 1849–1865.
- Ohlmann, J., D. Siegel, and L. Washburn, 1998: Radiant heating of the western equatorial Pacific during TOGA-COARE. *J. Geophys. Res.*, **103**, 5379–5395.
- Siegel, D., J. Ohlmann, L. Washburn, R. Bidigare, C. Nosse, E. Fields, and Y. Zhou, 1995: Solar radiation, phytoplankton pigments and the radiant heating of the equatorial Pacific Warm Pool. *J. Geophys. Res.*, **100**, 4885–4891.
- Skylingstad, E., W. Smyth, and G. Crawford, 2000: Resonant wind-driven mixing in the ocean boundary layer. *J. Phys. Oceanogr.*, **30**, 1866–1890.
- Skylingstad, E., W. Smyth, J. Moum, and H. Wijesekera, 1999: Turbulent dissipation during a westerly wind burst: A comparison of large eddy simulation results and microstructure measurements. *J. Phys. Oceanogr.*, **29**, 5–29.
- Smyth, W., D. Hebert, and J. Moum, 1996a: Local ocean response to a multiphase westerly windburst. part 1: The dynamic response. *J. Geophys. Res.*, **101**, 22495–22512.
- Smyth, W., D. Hebert, and J. Moum, 1996b: Local ocean response to a multiphase westerly windburst. part 2: Thermal and freshwater responses. *J. Geophys. Res.*, **101**, 22495–22512.
- Smyth, W., P. Zavialov, and J. Moum, 1997: Decay of turbulence in the upper ocean following sudden isolation from surface forcing. *J. Phys. Oceanogr.*, **27**, 810–822.
- Therry, G. and P. Lacarrere, 1983: Improving the eddy kinetic energy model for planetary boundary layer description. *Boundary Layer Meteorology*, **25**, 63–88.
- Troen, I. and L. Mahrt, 1986: A simple model of the atmospheric boundary layer; Sensitivity to surface evaporation. *Boundary Layer Meteorology*, **37**, 129–148.

Webster, P. and R. Lukas, 1992: TOGA COARE: The coupled ocean-atmosphere response experiment. *Bull. Am. Met. Soc.*, **73**, 1377–1415.

Weller, W. and S. Anderson, 1996: Surface meteorology and air-sea fluxes in the western equatorial Pacific Warm Pool during the TOGA Coupled Ocean-Atmosphere Response Experiment. *J. Climate*, **9**, 1959–1991.